ADVANCED MATERIALS TECHNOLOGIES
www.advmattechnol.de

Spike-based Self-Calibration for Enhanced Accuracy in Self-powered Pressure Sensing

*Chankyu Han, Jungrak Choi, Junseong Ahn, Hyunjin Kim, Ji-Hwan Ha, Hyeonseok Han, Seokjoo Cho, Yongrok Jeong, Jimin Gu, and Inkyu Park**

Self-powered pressure sensors are gaining popularity in human–machine interaction and mobile systems for their energy efficiency. Among the many types of self-powered sensors, triboelectric sensors have numerous advantages, including diversity of materials, ease of fabrication, and high voltage output. However, their signal is prone to be affected by both intrinsic and extrinsic factors including environmental change and discharging, which can significantly deteriorate the accuracy of measurement. To address this, a simple yet effective solution is proposed: a mechanically induced spike-based self-calibration method for a triboelectric pressure sensor. The sensor generates two signals: an open-circuit voltage and a spiking calibration voltage, enabling real-time calculation of current surface charge density. The calibration signal generates a spike at each predetermined discrete pressure change, whether positive or negative direction, denoting the corresponding direction of the pressure variation. This system successfully calibrates signals from various effects, including humidity change (20%–80%), discharging (over 10 days), and charge accumulation. This sensor has potential applications in precision agriculture for efficient crop harvesting and packaging in diverse environmental conditions.

1. Introduction

When 5G technology is commercialized in the near future, the amount of data transfer will increase tremendously and so will the amount of energy consumed.[1,2] Related applications such as smart farms and smart factories necessitate a large number of reliable and accurate sensors in operation all the time. Sensors based on passive mechanisms such as piezo-resistive[3–9] or piezo-capacitive[10–13] types require power from energy storage devices such as batteries. Since they require replacing and recharging due to restricted lifetime, there are growing research interests in self-powered sensors.

Among many types of self-powered sensors, triboelectric sensors have numerous advantages including diversity of materials, ease of fabrication, simple structure, and high voltage output. With the combination of contact electrification and electrostatic induction, triboelectric devices can generate electrical power and signal without requiring an external power source.[14] Owing to their self-powering characteristics and other merits, they are widely researched for a variety of applications such as ocean monitoring,[15–17] robotics,[18–23] smart healthcare,[24–29] and human-machine interaction.[30–35] Also, researchers are continuously working towards enhancing the energy density of triboelectric devices by innovating in materials, structures, and system compositions.[36–41]

However, a major drawback of triboelectric sensors is their low reliability due to their vulnerability to changes in environment, charging by contact electrification, and natural discharging behavior (**Figure 1**a,b). For pressure sensing, triboelectric signal, usually open-circuit voltage (V_{OC}), could be related to pressure due to the proportional relationship between the separation length (i.e. deformation) and V_{OC}. Theoretically, V_{OC} is proportional not only to the deformation but also to the surface charge density (σ) of triboelectric surfaces.[42] Humidity is a well-known influencing factor of surface charge density (Figure 1b(i)).[43–45] Meanwhile, other factors such as charging by contact electrification and discharging behavior are rarely discussed in triboelectric sensor literature. The working principle of triboelectric devices requires transfer of charges from one material to the other upon contact, known as contact electrification. This charging often takes more than single contact, and the transferred charges accumulate up to a certain saturation limit set by air breakdown.[38] Thus, when a triboelectric device is pressed successively or with higher pressure, the magnitudes of surface charge density and triboelectric signal increase (Figure 1b(ii)).[14,41] Moreover, surface charge density inherently decays with time although the decay rate may vary among materials (hours to days) (Figure 1b(iii)).[14,36,37,39] It was reported that the surface charge density can vary as large as a factor of 15 for the same triboelectric device.[41] Hence, a calibration

C. Han, J. Choi, J. Ahn, H. Kim, J.-H. Ha, H. Han, S. Cho, Y. Jeong, J. Gu, I. Park
Department of Mechanical Engineering
Korea Advanced Institute of Science and Technology (KAIST)
291 Daehak-ro, Yuseong-gu, Daejeon 34141, South Korea
E-mail: inkyu@kaist.ac.kr
J. Ahn, J.-H. Ha, Y. Jeong
Department of Nano Manufacturing Technology
Korea Institute of Machinery and Materials (KIMM)
156 Gajeongbuk-ro, Yuseong-gu, Daejeon 34103, South Korea
The ORCID identification number(s) for the author(s) of this article can be found under https://doi.org/10.1002/admt.202301199

DOI: 10.1002/admt.202301199

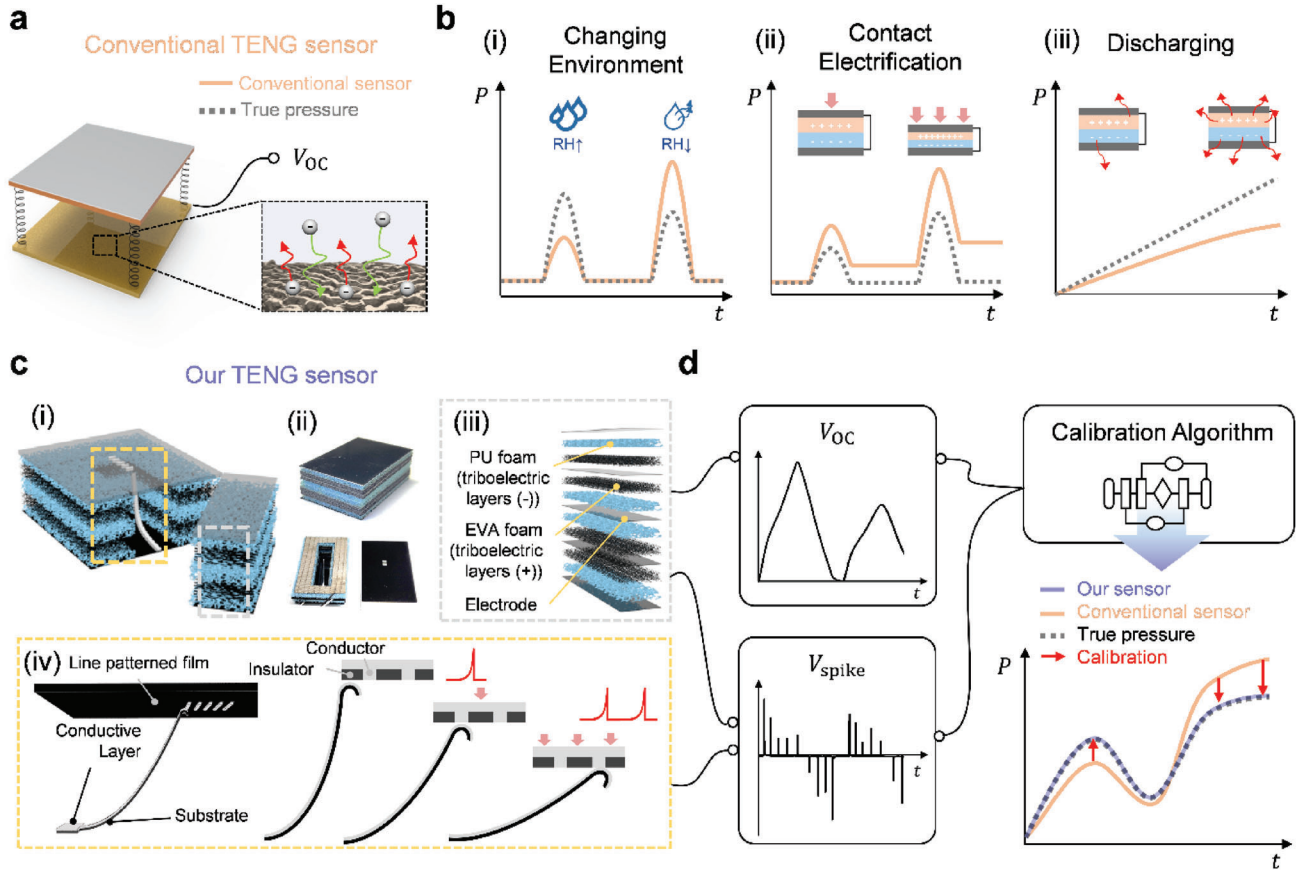

Figure 1. Concept of self-calibration and the overview of our sensor design. a) Unreliable signals from conventional TENG sensors due to changes in surface charge density (σ). b) Various factors influencing triboelectric signal (i.e. σ): i) changing environment, ii) contact electrification, and iii) discharging. c) Design of our self-powered triboelectric pressure sensor with self-calibration capability. i) A schematic illustration and ii) photographs of the fabricated sensor (top) and the sensor with the top electrode open (bottom). The sensor is composed of iii) a stack of porous triboelectric layers and iv) a geometrical switch. As the sensor is compressed, the beam slides on the electrode pattern, generating spike signals. This spike signal is utilized for our calibration process. d) Self-calibration of σ through simultaneous analysis of two signals, V_{OC} and V_{spike}, produced by the sensor in response to applied pressure Our calibration algorithm, removes the variability of σ, enabling accurate pressure measurements. Photo Credit: Chankyu Han and Jungrak Choi, KAIST.

method to compensate for the variability of sensor output from all influencing factors is vital for accurate measurements by triboelectric sensors.

Previously, there have been a few attempts to resolve this issue.[47–49] First, Jao et al. fabricated a triboelectric device with hydrogel to naturally remove the humidity effect on the output signal.[47] While σ decreases with increasing humidity, the conductivity of hydrogel increases due to water absorption. These effects counteract each other, resulting in an output signal that is not significantly affected by changes in humidity. However, the swelling characteristics of hydrogel are highly dependent on temperature, which poses a limitation to this approach. Secondly, Lee et al. fully packaged a triboelectric pressure sensor to eliminate the humidity effect.[48] Although the sensor successfully blocked the humidity effect, σ may still fluctuate due to other influencing factors including charging by contact electrification and discharging behavior. Lastly, Liu et al. developed an ingenious switchable operation method to circumvent the issue of changing σ.[49] This method involves subjecting a triboelectric device to alternating open-circuit and short-circuit conditions, which results in the production of current spikes.[50] The decay time constant of the generated spike is related to the pressure and independent of σ. However, the sensor has limited pressure resolution and requires a high sampling rate and an externally powered transistor as a switch. Additionally, the motion of interest has to be comparable to a fixed switching frequency. To the best of our knowledge, there has been no prior research that has been able to simultaneously compensate for the variability of σ from all influencing factors and achieve a high-resolution signal.

Herein, we propose a spike-based self-calibration for a triboelectric self-powered pressure sensor that enables real-time calculation and compensation of surface charge density for accurate and reliable measurements (Figure 1c). Our sensor is able to compensate for the variability of σ from all influencing factors. Our sensor produces two voltage signals: V_{OC} and spiking calibration voltage (V_{spike}). Just as other conventional triboelectric devices, V_{OC} responds not only to the change in pressure but also to the change in surface charge density. However, V_{spike} produces pressure-encoded timed spikes that are independent of σ, based on geometrically switchable operation. We developed a

calibration algorithm with inputs of V_{OC} and V_{spike} to calculate σ in real-time and calibrate sensor signal to be independent of all factors influencing σ, which includes humidity, charging, and discharging (Figure 1d). Thus, the sensor can self-calibrate in response to the change in σ: it does not require external calibration instruments and manual calibration procedures by users. Owing to its insensitivity to the change in σ, the pressure sensor is applicable to accurate and reliable sensing applications such as smart farms and field robotics. As a demonstration for precision agriculture, a robotic arm equipped with our triboelectric pressure sensor safely harvested crops in diverse environmental conditions based on the calibrated measurement, and the weight of crops in a packaging box could be accurately measured. This work would pave the way for enhanced reliability and accuracy of self-powered sensing technology, independent of extrinsic and intrinsic factors.

2. Results and Discussions

2.1. Design of Self-Powered Pressure Sensor with Self-Calibration Capability

Our self-powered pressure sensor consists of two parts: the triboelectric part and the electrical switch part (Figure 1c, Figure S1, Figure S2, Supporting Information). As triboelectric materials, porous polyurethane foams (PU) and porous ethylene-vinyl acetate foams (EVA) are utilized owing to their high triboelectric performance (Figure 1c(iii)).[51] Porous materials are used because the performance of triboelectric devices increases with the increase in porosity of triboelectric materials.[52] This is a synergetic effect of increase in triboelectric charge density and an increase in dielectric constant upon closure of pores. As the porous triboelectric material is compressed, charge is not only transferred at the contact surface but also induced at the surfaces of pores away from the contact surface due to electrostatic induction.[52] Moreover, as dielectric constants of PU and EVA are higher than that of air, the closure of air pores upon compression leads to an increase in dielectric constant and corresponding capacitance between electrodes. As a porous structure ensures large elastic compressive strain,[53] the sensor does not require spacers to separate the triboelectric materials, which simplifies the overall sensor design and fabrication process. The electrical switch part is composed of an electrically conductive mechanical beam and a plate with an alternating parallel-line pattern of insulator and conductor, as illustrated in Figure 1c(iv). The switch is connected at certain geometrical conditions only to achieve geometrically switchable operation which will be discussed in more detail in the next section.

2.2. Self-Calibration Spike Generation Based on Geometrically Switchable Operation

The basic principle of triboelectric pressure sensors is illustrated in Figure S3 (Supporting Information). When a PU layer and an EVA layer are in contact, charge transfer occurs. Even when they are separated, the charge remains on the *transferred* surfaces. By attaching electrodes, electrical signals corresponding to the separating and approaching motions are generated without external power. There are two major methods to measure the electrical signal: open-circuit voltage (V_{OC}) and short-circuit current (I_{SC}). If the two electrodes are disconnected, the voltage between the electrodes changes with the relative displacement of two layers. The V_{OC} is proportional to both the separation length and surface charge density:

$$V_{OC} = \frac{\sigma(t)\ x(t)}{\varepsilon} \tag{1}$$

where x(t) is the separation length, and ϵ is the electric permittivity between the electrodes.[42] Also note that the surface charge density (σ) is a variable that can change in time due to various factors, which will be further discussed later. If the two electrodes are connected, infinitesimal motion creates a small voltage; charge is redistributed to equalize the electric potentials of the electrodes, which creates an abrupt current flow. The I_{SC} is proportional to the speed of motion and surface charge density.[42]

Figure 2a shows the mechanism of the self-powered spike generation by utilizing a geometrically activated electrical switch and a triboelectric sensor. When the triboelectric sensor is in switchable operation, which is alternating condition between open-circuit and short-circuit, V_{OC} is generated with its motion during open-circuit condition, and corresponding abrupt current spike is generated when the condition changes to a short-circuit.[49,50] The current spike decays exponentially to zero, as in a circuit with a resistor and a charged capacitor in a parallel connection. Connecting the electrodes of a triboelectric sensor to the geometrical switch, geometrically switchable operation is realized. With a sufficient amount of V_{OC} accumulated between consecutive short-circuit conditions, an observable current spike is generated at every strain increment or decrement, defined by the geometrical switch. Additionally, as V_{OC} is generated in opposite directions upon compressing and releasing motions, current spikes are also generated in opposite directions depending on the direction of motion.

As highlighted in red in Figure 2a, the geometrically switchable operation requires an electrical switch that is activated only on the particular geometrical conditions of the sensor. For example, the switch is connected and disconnected every 10% strain increment. Figure 2b provides an illustration of such a switch composed of a conductive beam sliding on a parallel-line patterned plate. As the plate moves down, the beam slides on the bottom surface of the plate (Figure 2c and Movie S1, Supporting Information). As the beam is conductive, the beam and plate alternate between electrically connected and disconnected states. Therefore, they work as an electrical switch that is connected at certain geometrical conditions only. The mechanical beams were produced by pressing aluminum (Al) foil and half-cured carbon fiber reinforced polymer (Al/CFRP), laser-cutting it to the desired 2D shape, and co-curing it in the 3D printed mold (Figure S4, Supporting Information). CFRP was utilized as a substrate material because of its high modulus, wide elastic range, and excellent fatigue resistance.[54] The numerical simulation supports that the deflection of the beam is within the elastic region: the maximum local strain of the beam is only 0.76% when the sensor is compressed by 35% (Figure S5, Supporting Information). The top plate with a parallel-line pattern was fabricated by laser ablation of an anodized Al plate (Figure S6, Supporting

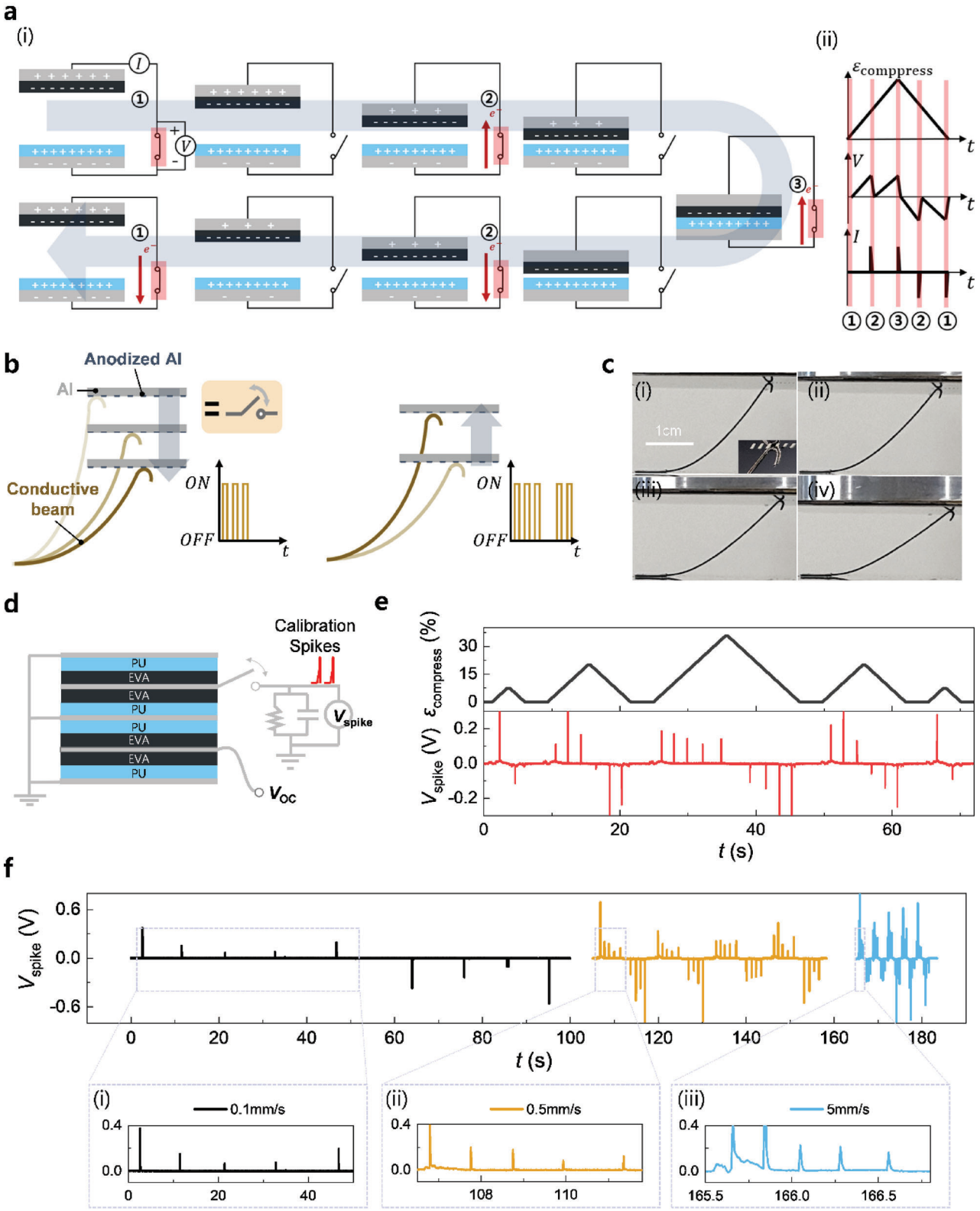

Figure 2. Geometrically switchable operation for generation of calibration spike signal. a) A working principle of geometrically switchable operation: i) A schematic illustration of compression cycles with a geometrical switch connected to the electrodes of a TENG device. The red highlights indicate short-circuit condition of the geometrical switch (i,ii). ii) Corresponding voltage and current signals for a compression cycle. b) A conceptual illustration of the geometrical switch. As the top plate with alternating patterns of conductor (aluminum) and insulator (anodized aluminum) moves down, the

Information). A detailed description of the switch dimension, fabrication process, and fabricated result is presented in Figures S7 and S8 and Movie S2 (Supporting Information). The fabricated electrical switch could alternatively connect and disconnect ten times per compression cycle with a maximum strain of 35% (Figure S9, Supporting Information).

To demonstrate the spike generation, the stack of triboelectric materials with corresponding electrodes and the measuring circuit were set up as illustrated in Figure 2d. The resistor and the capacitor were connected in order to match the time scale of each spike to the sampling frequency for stable measurement (Figures S10 and S11, Supporting Information). The stack was compressed and released at three different compressive strains (Figure 2e). Each spike indicates a certain increment or decrement in the compressive strain. The larger motion produced a larger number of spikes since the electrical switch was activated more. The spikes were generated in a positive and negative direction upon compression and release, respectively. Counting the number of spikes up and down enables the approximation of pressure. Figure 2f shows the result of spike generation for the same compression cycles with various speeds of motion. Unlike the speed proportionality of I_{SC}, the magnitudes of spikes in V_{spike} were not significantly affected by the speed variation by a factor of 50, from 0.1 mm s^{-1} to 5 mm s^{-1}. However, slight variations in magnitudes of spikes can be observed within a cycle and between cycles. The difference within a cycle is due to the nonlinearity in both V_{OC} and switch activation with respect to the compressive strain. The magnitude difference between cycles is due to the randomness of the contact resistance at the initial contact between the beam and the conductive pattern. However, any differences in the size of the spikes are not important, as long as they exceed a particular threshold, since it is the timing of the spike's activation that carries the calibration information, rather than its magnitude.

2.3. Calculation of Surface Charge Density

Figure 3a shows that σ of triboelectric sensor can change in time due to various factors. Humidity is one major factor (Figure 3a(i)). When humidity is high, the adsorption of water molecules on the surfaces of triboelectric layers leads to a decrease in σ.[43,55] Another major factor is charging by contact electrification (Figure 3a(ii)). Triboelectric signal is generated by the relative displacement of charged layers, where the charge is accumulated resulting from contact electrification. However, the charge transfer is usually not completed after a single contact. The quantity of charge transferred rises as the number of contacts increases or the contact force intensifies until reaching the saturated state.[41] The maximum charge density is limited by air breakdown when air begins to conduct electricity due to the applied electric field exceeding the dielectric strength of air.[38] Another major effect is the discharge of the material over time, as shown in Figure 3a(iii). Once the material has become charged, it will gradually discharge in the absence of any additional contact electrification. The rate of decay can differ widely depending on the material, ranging from hours to days.[37,39]

When the σ of a triboelectric sensor changes, the magnitude of the corresponding signal also changes proportionally, as shown in Equation 1. Thus, the low reliability of triboelectric signal is due to the change in σ. As humidity is one of the primary factors that affect σ and is relatively easy to control, we placed our sensor in a humidity chamber to investigate the effect of σ on the sensor's signal (Figure S12, Supporting Information). The relative humidity (RH) of the chamber was controlled from 20% to 80% at 22 °C with a humidifier, and the corresponding sensor response to compression cycles was measured as displayed in Figure 3b. Although the overall magnitudes of V_{OC} decreased significantly with the increase in humidity, the timing pattern of the spikes in V_{spike} remained the same in all humidity conditions. If σ is known, the susceptibility of triboelectric signal to the humidity can be compensated and eliminated.

Figure 3c outlines the method for calculating σ using the reference data set and the change in V_{OC} between two consecutive spikes in V_{spike}. Notably, the timing pattern of spikes in V_{spike} is independent of σ. However, the magnitude of V_{OC} can vary due to changes in σ. Although the variability of σ that leads to variability of V_{OC} is unavoidable, V_{spike} provides useful information to calculate σ. It is because the geometrical condition of the sensor is known at the exact moment when a spike is generated in V_{spike}. By assigning a transition number, i, to each spike and calculating the change in V_{OC} between the two consecutive spikes, the ratio of σ relative to the reference σ can be determined. For instance, the ΔV_{OC} of the current sensor at a given RH level is divided by the ΔV_{OC} of the reference data at the same transition number to obtain σ_{RH}/σ_{ref}. A detailed explanation of surface charge density calculation is given in text S1.

Figure 3d depicts the relationship between $|\Delta V_{OC}|$ and the transition number, i, for different humidity conditions. Throughout all levels of humidity, a consistent trend is observed, albeit with fluctuations in the values depicted on the y-axis. If there is no change in σ, the $(\Delta V_{OC})_i$ should be invariant, because V_{OC} is directly related to the deformation of the sensor (Equation 1) and each transition number corresponds to specific geometrical change of the sensor. However, since V_{OC} is also related to σ, the variation of $(\Delta V_{OC})_i$ is due to the variation in σ. The reference data is obtained by averaging the $|\Delta V_{OC}|$ values at all humidity conditions for each transition number and is differentiated from other data by a dashed line in the Figure. Also note that for $i = 1$, the ΔV_{OC} is defined as the change in V_{OC} from the zero-value

conductive beam bends and slides on the patterned plate. It results in an alternation between short-circuit and open-circuit that depends only on the geometrical state of the sensor. c) Camera images of the conductive beam sliding on the patterned plate under compression. The inset in (i) shows the magnified view of the patterned electrode in contact with the beam. d) The circuit design for measurement of the calibration spike signal (V_{spike}) and the open-circuit voltage (V_{OC}). e) Spike generation for five cycles with varying maximum compressive strain. As the sensor is pressed and released with more strain (i.e. higher pressure), the number of spikes both upward and downward increases. f) Speed independence of V_{spike}. The sensor was compressed up to same maximum pressure. The insets show the magnified plots of V_{spike} at i) 0.1mm s^{-1}, ii) 0.5mm s^{-1}, and iii) 5mm s^{-1}. The magnitudes of spikes are independent of speed. Photo Credit: Chankyu Han and Jungrak Choi, KAIST.

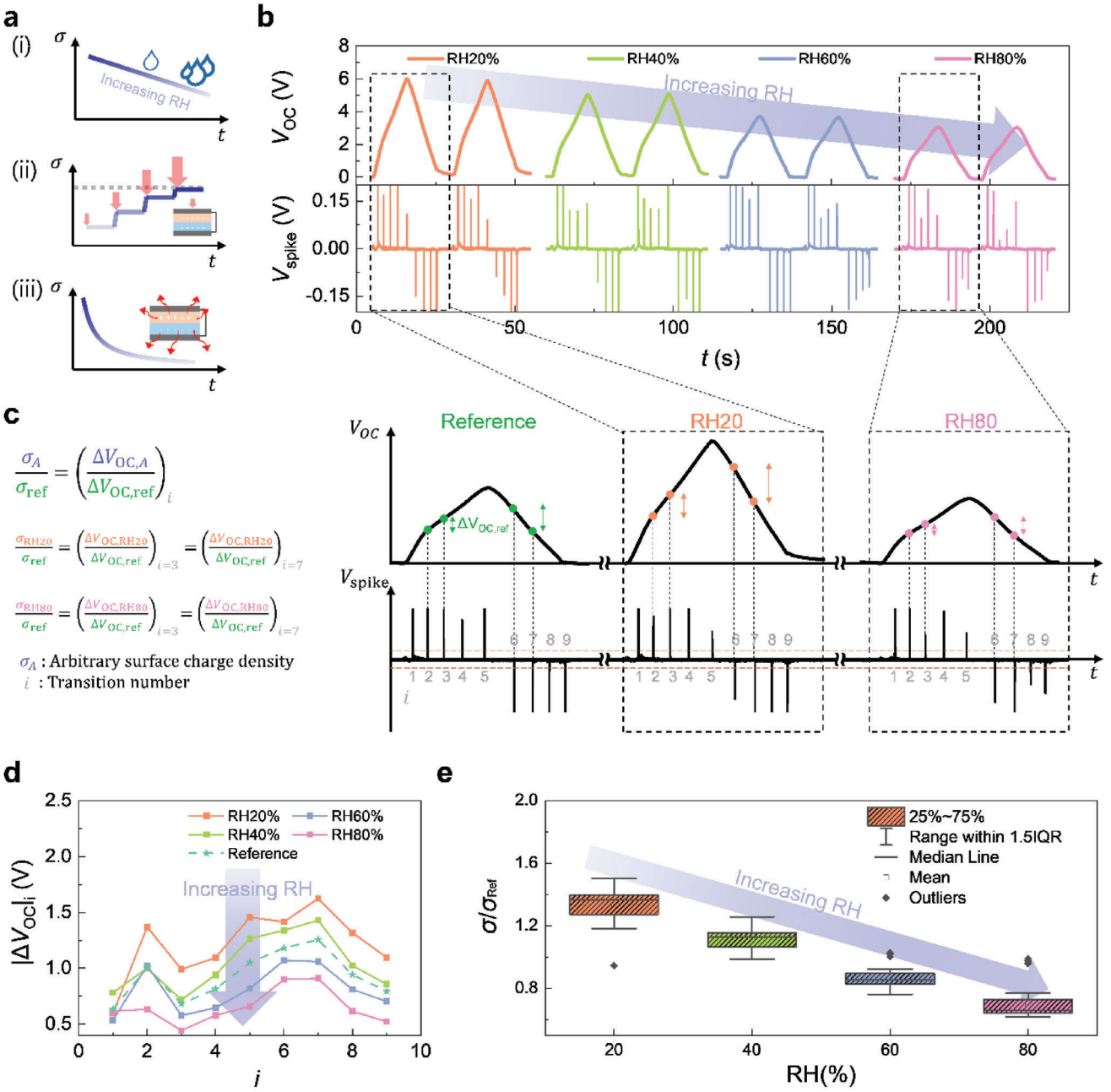

Figure 3. Calculation of surface charge density (σ/σ_{ref}) based on calibration spike signal (V_{spike}) and open-circuit voltage (V_{OC}). a) Three major factors that influence σ: i) humidity, ii) charging by contact electrification, and iii) discharging. b) Raw sensor signals (V_{OC} and V_{spike}) for compression tests at four different humidity conditions with the same maximum pressure. While V_{OC} decreased with increasing relative humidity (RH) (i.e. decreasing σ), the timing patterns of spikes in V_{spike} were independent of RH. c) Main principle of σ/σ_{ref} calculation. The comparison of the change in V_{OC} with the reference data of the same transition number, i, enables calculation of σ/σ_{ref}. d) Change in open-circuit voltage at specific transition number, i. Reference data is obtained by averaging the values from four humidity conditions at each i.e.) Calculated surface charge densities at four humidity conditions. e) The calculated surface charge density decreased with increasing RH and can be used for self-calibration process. IQR denotes an interquartile range.

(i.e. rest position). The calculated σ for each humidity condition, based on the mechanism explained in Figure 3c, is presented as a box plot in Figure 3e. As expected, σ/σ_{ref} decreases from 1.326 to 0.702 as RH increases from 20% to 80%. It is important to note that the humidity data itself is not used as an input to calculate the surface charge density. Moreover, the σ/σ_{ref} calculation algorithm is applicable in humidity conditions other than RH 20%, 40%, 60%, and 80% or σ-varying situations caused by other factors, such as discharging and contact electrification, as demonstrated in the subsequent section.

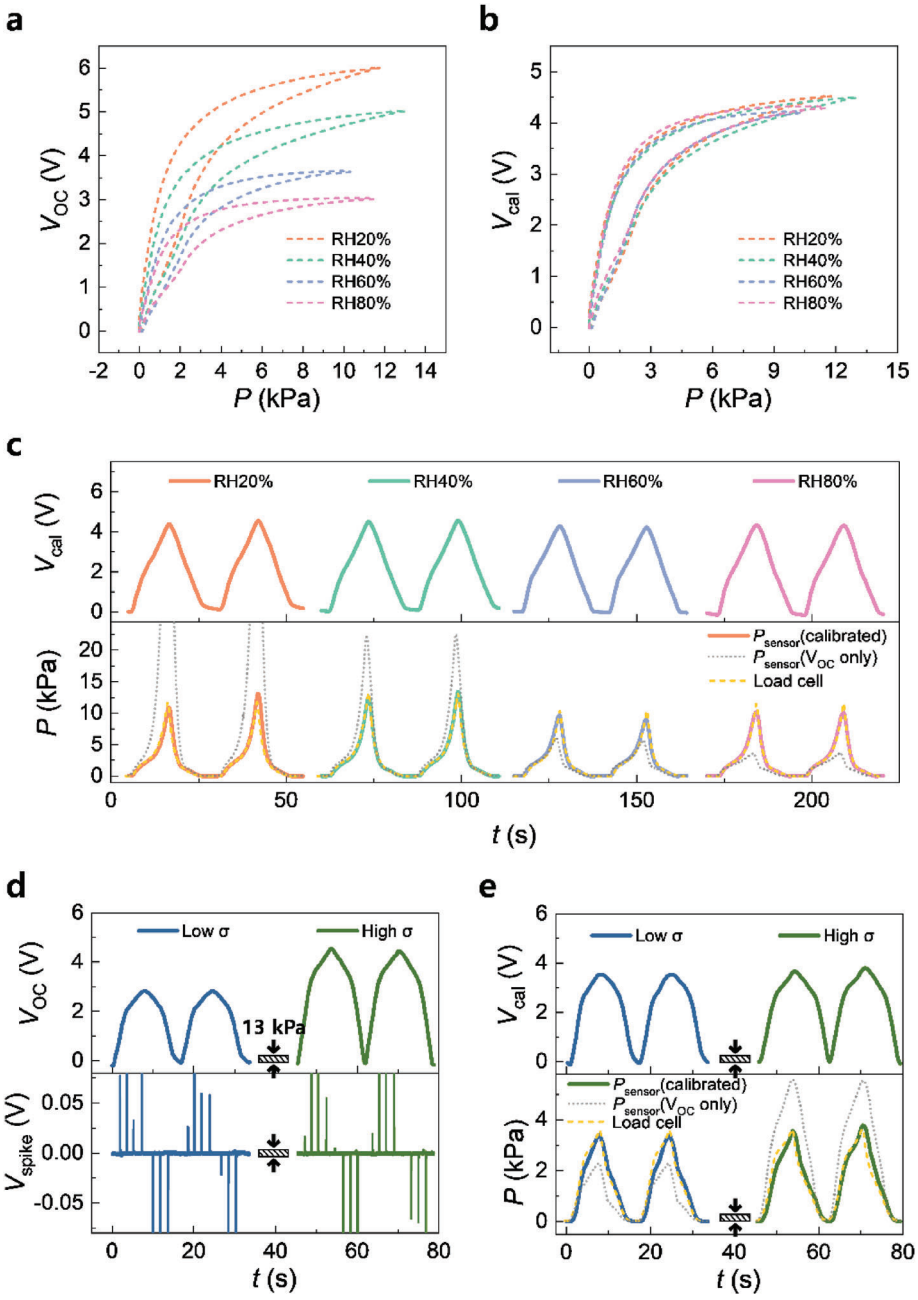

Figure 4. Pressure sensing performance based on self-calibration method. a) Dependence of open-circuit voltage (V_{OC}) on humidity at various pressures, indicating that V_{OC} decreases as humidity increases. b) Independence of calibration spike signal (V_{spike}) on humidity at various pressure. With the σ/σ_{ref} calculated from our calibration algorithm, V_{cal} is obtained by dividing V_{OC} by σ/σ_{ref}. c) Calibrated sensor signals on different humidity conditions. Real-time calibration is possible. Although pressure inferred from V_{OC} only significantly overestimates pressure at low relative humidity (RH) and understates at high RH, pressure calculated from V_{cal} matches well with the true pressure. d) Raw sensor signals (V_{OC} and V_{spike}) for compression cycles with same maximum pressure before and after deliberate charging with strong compression of 13 kPa. The magnitude of V_{OC} increased by a factor of two after the charging process, highlighting the need for calibration. e) Calibrated sensor signals based on the self-calibration method that effectively corrects the sensor signals and resolves the under- and over-estimation of pressure caused by deliberate charging.

2.4. Real-Time Self-Calibration of Surface Charge Density

Based on the calculated σ/σ_{ref}, V_{OC} can be calibrated, and pressure can be inferred from this calibrated voltage (V_{cal}) regardless of the change in σ. As V_{OC} is proportional to σ (Equation 1), V_{cal} can be obtained by dividing V_{OC} by σ/σ_{ref}. **Figure 4**a plots the V_{OC} with respect to pressure at four distinct humidity conditions. The V_{OC} at 11.5kPa are 5.98V and 3.01V under RH 20% and RH 80%, respectively. They differ by a factor of almost two, which means that the inference of pressure from V_{OC} alone is

inaccurate. On the other hand, Figure 4b plots V_{cal} with respect to pressure at four humidity conditions. The calibration was successful as the graphs from different RH's overlapped well. Essentially, as shown in Equation 2, the calibration process replaces the variable $\sigma(t)$ in Equation 1 with a constant, σ_{ref}. The V_{cal} can be further converted to pressure based on curve fitting (Figure S13, Supporting Information).

$$V_{cal} = V_{OC} \times \frac{\sigma_{ref}}{\sigma(t)} = \frac{\sigma_{ref}\, x(t)}{\varepsilon} \quad (2)$$

This self-calibration process is performed in real-time. As σ/σ_{ref} is calculated for each spike, this approach enables the sensor system to dynamically calibrate the sensor signal to account for changes in σ. To reduce the fluctuation of V_{cal}, the moving average of the latest five calculated σ/σ_{ref} values was utilized to calculate V_{cal}, and the divided result was filtered by a low-pass filter. The flowchart of the calibration algorithm is provided in Figure S14 (Supporting Information). As shown in Figure 4c, the sensor could successfully calibrate and convert the sensor signal to pressure. Without calibration, the inference of the pressure significantly over- or under-estimated due to the change in σ from the variation in humidity (Table S1, Supporting Information). Although PU/EVA pair was selected for our sensor, other triboelectric materials may also be utilized as long as they can also generate observable spikes in V_{spike}. A sensor made of Nylon/EVA pair was also tested in varying humidity conditions that also resulted in successful self-calibration (Figure S15, Supporting Information). Therefore, our calibration process is not only applicable to our specific sensor but can also be applied broadly to sensors of other materials and configurations under one condition: observable spike generation in V_{spike}.

By directly computing the ratio of current σ to the reference value, our self-calibration method is capable of calibrating the sensor output from factors beyond humidity. To deliberately reduce σ, we discharged our sensor for a period of ten days, following which we recorded the sensor response to compression cycles with a maximum pressure of 3.8 kPa before and after intentionally charging the sensor by applying high pressure of 13 kPa (as depicted in Figure 4d). The compression cycles with a low maximum pressure of 3.8 kPa were performed to demonstrate that such dramatic change in σ is possible depending on charging and discharging. If the sensor was tested with high maximum pressure, it would have been charged when performing the test. The difference in magnitudes of V_{OC} before and after charging process is as significant as the difference due to humidity variation ($V_{OC,before}$ = 2.8 V and $V_{OC,after}$ = 4.5 V at 3.6 kPa). Nevertheless, the V_{spike} provided the same timing patterns of spikes for both cases. Thus, utilizing our calibration algorithm, the pressure could be accurately estimated from V_{cal}, while relying solely on V_{OC} resulted in significant underestimation or overestimation of pressure (as shown in Figure 4e). Additionally, the sensor was left to discharge for another ten days. Then, the sensor was repeatedly pressed with the same compression cycles. Although the magnitudes of V_{OC} increased every cycle until saturation, the deviation in V_{cal} was largely suppressed by self-calibration (Figure S16, Supporting Information). Therefore, our sensor system can provide accurate pressure values regardless of the change in σ from various factors.

In terms of sensor characterization, the sensitivity of the sensor varies depending on the amount of surface charge density from 1.25 V kPa^{-1} to 0.75 V kPa^{-1} when humidity increases from RH 20% to 80% (Figure 4a). The sensing range was set to be up to 12 kPa due to the decreasing sensitivity at high-pressure values. The detection limit is governed by the geometrical condition at which the first spike is generated because the sensor signal is unreliable before self-calibration. The fabricated sensor produces the first spike upon compression at 0.8 kPa. However, this detection limit can be further reduced by the intricate alignment of the beam and the patterned top electrode. Other sensor characterization results including dynamic charge output, fast response time, and long-term stability are provided in Figures S17–S19 (Supporting Information). It was also shown also that the beam has a negligible effect on the mechanical property of the assembled sensor because the bending stiffness of the beam is negligible compared to the compressive stiffness of the porous materials (Figure S20, Supporting Information).

2.5. Demonstration for Smart Farm Sensor Applications

As illustrated in **Figure 5**a(i), a smart farm is a farming system combined with modern Information and Communication Technologies (ICT), Internet of Things (IoT), big data analysis, and robotics. One of the essential technologies of smart farms is environmental control because each crop type has specific environmental conditions for optimal growth, including the optimal RH ranging from 50% to 90%.[56–58] Based on sensor technology, big data analysis, and actuation system, many have succeeded to grow crops in a compact area with optimal output. However, the current smart farm still requires human labor, and unmanned smart farms filled with farming robots and drones are desirable for their prolonged operation time and efficient usage of space.[59] Such robots should be able to accomplish various tasks such as seeding, harvesting, and packaging (Figure 5a(ii,iii)). Among them, harvesting crops requires delicate control of the robotic gripper to maintain a certain level of pressure to avoid dropping or damaging the crops.

Our self-powered triboelectric pressure sensor can be applied to farming robots to harvest various crops regardless of the changing humidity conditions (Figure 5b). To demonstrate this, a cherry tomato and lettuce were grabbed, transported, and released by a robotic arm based on our calibrated sensor signal. If conventional triboelectric pressure sensors were utilized, the crop would have been damaged by dropping or squeezing too hard due to the over- or under-estimation of the pressure, respectively. At an optimal RH of 75% for lettuce, conventional triboelectric sensors would underestimate the pressure, potentially causing excessive grasping force. Conversely, in the case of cherry tomatoes, which require an optimal RH of 55%, the sensor may overestimate the pressure, resulting in a loose grip and dropping of the crop. However, our sensor system can calibrate the triboelectric signals at various σ caused by the RH change. For the demonstration, the sensor was further packaged with shielding and protective layers to avoid unwanted excessive moisture intrusion into the sensor that can deteriorate the sensor output (Figure S21, Supporting Information). The target holding pressure was set to 1.6 kPa for both crops, which ensures a firm

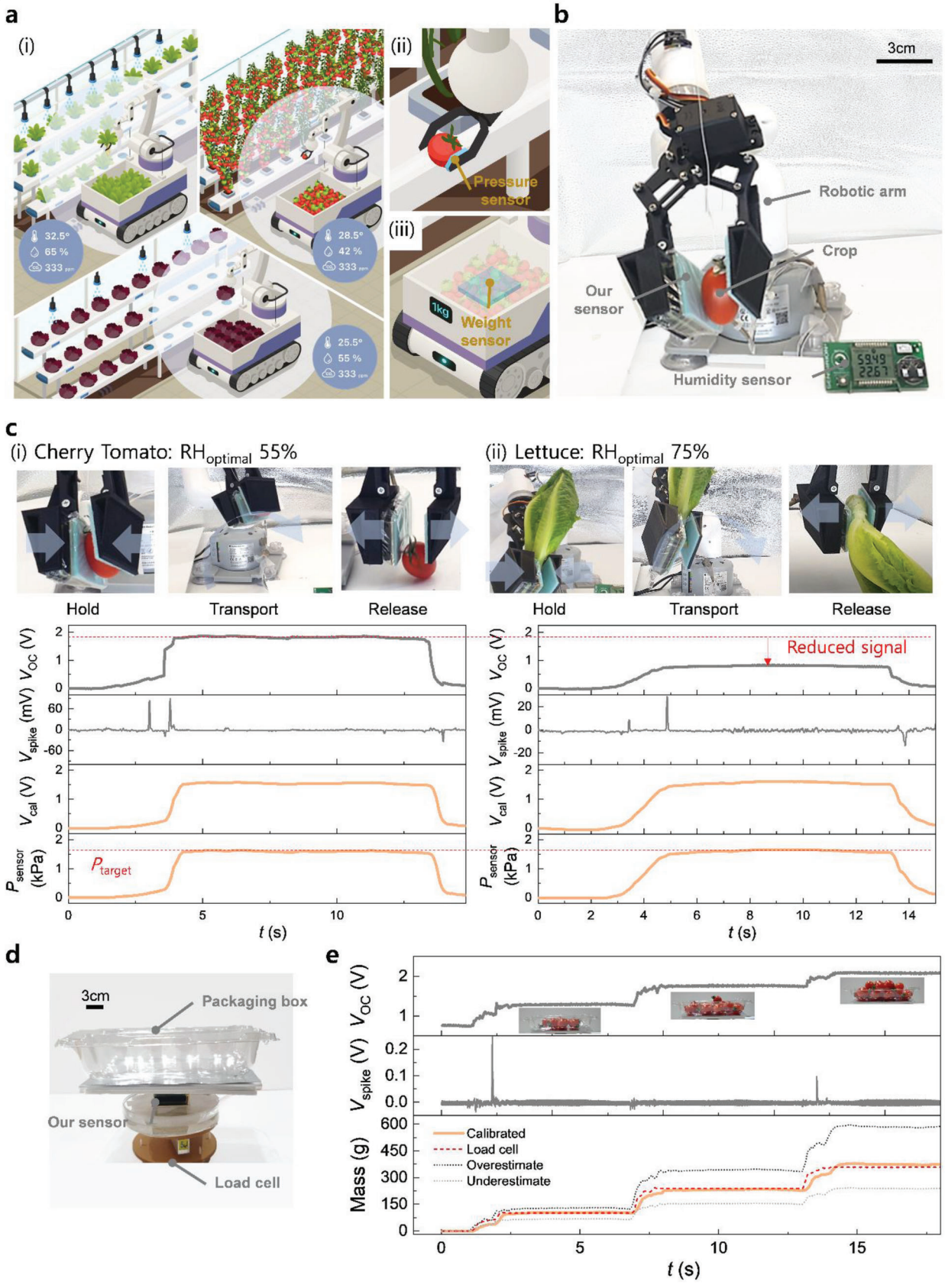

grip without damage. However, as cherry tomatoes have lower optimal RH than lettuce, the triboelectric signal at the target pressure was higher for cherry tomatoes. As shown in Figure 5C and Movie S3 (Supporting Information), our system could successfully compensate for variability in σ. While crops were held with the same target pressure, the holding V_{OC} for cherry tomatoes, 1.9 V, was much higher than that for lettuce, 0.85V. Without the calibration, it is impossible to know that these two signals indicate the same pressure value.

Furthermore, the sensor can be utilized as a self-powered weighing sensor. After harvesting crops, they need to be packaged into a box with a fixed amount. Our sensor was placed under the packaging box on top of a commercial load cell (Figure 5d). While cherry tomatoes are poured into the box, the sensor performs calibration at each spike and accurately calculates the weight. In the demonstration (Movie S4, Supporting Information), cherry tomatoes were poured into the packaging box by three times. While one spike was observed for the first and third pouring each, the second one did not add sufficient weight to activate the spike (Figure 5e). The weight measurement from our calibrated sensor matched well with the measurement from the reference load cell. If the raw V_{OC} was utilized for weight measurement, the weight would have been underestimated. Otherwise, if the V_{OC} were higher by 30%, which is within the practical variation range due to humidity and charging/discharging, the pressure would have been significantly overestimated without calibration (Figure 5e). This would have led to an excessive or insufficient amount of tomatoes in the box. As the sensor is lightweight (<5 grams), this sensor can be directly mounted on mobile robots so that they can perform harvesting and packaging at the same time. Such incorporation of self-powered sensors will increase the sustainability of smart farms.

3. Conclusion

Our study identifies three key considerations. First, design diversity for the geometrical switch is possible depending on the target application. We achieved geometrically switchable operation by combining an electrically conductive beam with a plate featuring a conductive parallel lines pattern. During compression, the beam slides along the patterned plate, alternating between short-circuit and open-circuit conditions. Different designs for geometrical switches, beyond sliding beams on a patterned plate, could lead to triboelectric systems with distinct forms and purposes that still produce spike signals, indicating the current state of the system independently of σ. Second, the maximum detectable speed of motion is an important factor to consider. Since discrete counting of spike signals in V_{spike} is required, the sampling rate of V_{spike} determines the maximum operation speed. In our study, the sampling rate was set to 100Hz, meaning that two spikes generated within 0.02 s would be counted as a single spike. Thus, the sampling rate of V_{spike} should be selected with the maximum speed of input motion in mind. Lastly, while porous foams were used in this study, the geometrically switchable operation is feasible with other triboelectric materials. The only requirement is that sufficient V_{OC} must accumulate between two consecutive short-circuit conditions to produce an observable spike signal. We believe that this mechanism could be applied to various other situations and applications.

In summary, we have developed a self-powered pressure sensor with a self-calibration feature to compensate for changes in surface charge density. By generating a series of spikes that encode pressure information through geometrically switchable operation, our sensor can calculate and calibrate changes in surface charge density in real time, even in conditions of varying relative humidity, time decay, and charge accumulation from repeated or strong contact electrification. Additionally, we demonstrated the use of our sensor in smart farming scenarios, including crop harvesting and packaging. To further enhance the technology, potential areas for improvement include optimizing the triboelectric material and electrode patterns for spike signals, studying the variability of triboelectric simulations, and implementing additional functionalities such as circuits and packaging systems. We believe that our approach can be extended to various self-powered sensing applications, leading to the development of more sustainable and robust sensor systems.

4. Experimental Section

Fabrication of the Geometrically Activated Electric Switch: The electrical switch was composed of two parts: an electrically conductive mechanical beam and a parallel-lines patterned plate. First, an Al foil was placed on top of half-cured unidirectional carbon fiber reinforced polymer (CFRP) (USN150A, SK Chemicals, Korea), and it was pressed with a pressure of 1 MPa for 1 min by a pneumatic press machine. The CFRP/Al composite was cut to a desired shape using a laser machine. The long direction of the beam was parallel to the direction of carbon fiber. The male and female molds of the desired beam shape were produced by a Digital Light Processing (DLP) 3D printer (Phrozen Technology, Taiwan). The shape of the beam curve was set to be parabolic. The cut CFRP/Al composite was placed on the female mold and pressed by the male mold with Al side facing upwards. The entire mold with CFRP/Al composite was placed inside a convection oven at 120 °C for 1 h. After curing, the beam was removed from the molds. Second, an Al plate with an anodized surface was engraved by the laser machine. The anodized surface was removed by laser ablation leaving a parallel-lines pattern. The width of line was set as 150 μm, and the spacing between lines was 550 μm. The depth of the ablated region was measured as 10 μm by Vernier calipers.

Fabrication and Integration of the Sensor: Porous polyurethane (PU) foam and ethylene-vinyl acetate (EVA) foam with a thickness of 2 mm

Figure 5. Self-calibration of pressure sensors in smart farm scenarios. a) Schematic illustration of a smart farm. i) Conceptual overview of mobile robots in smart farms. ii) Mobile robots harvest crops based on pressure sensor data, iii) with subsequent weight measurement for on-board packaging. b) The experimental setup for crop harvesting. Humidity sensor is present only to notify the current humidity to viewers; the humidity data was not used for the calibration procedure. c) Successful crop harvesting using a self-calibrated sensor signal to control a robotic gripper. The holding pressure was set to the target pressure of 1.6 kPa for both crops. The calibration algorithm successfully calculated the pressure to grab the lettuce with the desired pressure, despite the open-circuit voltage (V_{OC}) dropping due to the lettuce's high optimal relative humidity (RH). d) Usage of the calibrated sensor response to weigh products for packaging. Cherry tomatoes were poured into a plastic packaging box. e) Sensor signals of pouring a chunk of cherry tomatoes three times, with two spikes observed. Calibration enabled accurate weight estimation, which could have been under- or over-estimated without calibration. Photo Credit: Chankyu Han and Jungrak Choi, KAIST.

were cut into 35 mm × 53 mm with a 10 mm × 35 mm hole at the center. A 100 µm thick double-sided Al conductive tape was cut into identical sizes but with a 1 mm offset toward the inner part. Each layer was made up of either PU or EVA material and adhered to both sides of the tape. The layers were arranged in an alternating pattern, consisting of three layers of each material (PU and EVA). An anodized Al plate was cut into 35 mm × 53 mm, and the conductive beam was adhered to a designated position. At the bottom of triboelectric stack, the plate with the beam was adhered, and the parallel line patterned anodized Al plate was adhered to the top. The conductive beam was electrically connected to one of the electrodes of EVA layers.

Electric Measurement And Characterization of the Sensor: The open-circuit voltage (V_{OC}) was measured using an electrometer (Keithley 6514, Tektronix, USA). The calibration spike voltage (V_{cal}) was measured using a data acquisition system (DAQ) (USB-6211, National Instruments, USA). The calibration spike voltage signal line was parallelly connected to 1) an analog input port of the DAQ, 2) a resistor (10 MΩ), and a capacitor (500 pF), which were connected to ground in parallel. All measurements (V_{OC} and V_{spike}) were monitored and recorded by LABVIEW software (National Instruments, USA) in a PC, which was connected to the electrometer and DAQ. The mechanical properties of the sensor were measured using a universal testing machine (AGS-X, Shimadzu, Japan). To obtain the sensor response to various pressures and speeds of motion, the universal testing machine was utilized to apply desired strain or pressure with desired speed. The experiments were conducted with a strain rate of 0.029 s^{-1} and speed of 0.5 mm s^{-1} except for those with other specified strain rates. Movie S5 (Supporting Information) provides a video of applying cyclic loading on the sensor and measuring the V_{OC} and V_{spike} with a PC.

Humidity Control: An acrylic chamber was built to fit the universal testing machine. The humidity inside the chamber was controlled by connecting a hose from a humidifier to the chamber. The relative humidity of the chamber was measured by a humidity sensor (Sensirion AG, Switzerland).

Real-Time Surface Charge Density Calibration: For the real-time calculation and calibration of σ, the algorithm was run by LabVIEW while simultaneously receiving the V_{OC} and V_{spike} from the electrometer and DAQ. A spike was detected when the absolute value of V_{spike} exceeded a threshold voltage, which was set by multiplying a safety factor (2.5 in this study) by the maximum noise level at rest. The pressure level was determined by the direction of the spike, with each upward spike increasing the pressure level by one, and each downward spike decreasing the pressure level by one. The change in V_{OC} between current and previous spiked moments were calculated and divided by the corresponding reference data based on the transition number. To determine V_{cal}, the σ/σ_{ref} was obtained using a five-value moving average calculation, and then V_{OC} was divided by the resulting σ/σ_{ref}. Then, V_{cal} was converted into pressure based on a predefined nonlinear fitting curve. The flowchart for the algorithm was given in Figure S14 (Supporting Information).

Finite Element Simulation: Finite element analysis (FEA) was conducted to estimate the kinematics of the beam when a flat top plane moves down with frictionless contact. Abaqus software (Dassault Systemes Simulia Corporation, Johnston, RI) was utilized for this simulation. The purpose of this simulation was to obtain the trajectories of contact points between the beam and the top plate during the downward motion from different beam shapes.

Smart Farm Application Setup: A robotic gripper with a high-torque servo motor was mounted on a robotic arm (Elephant Robotics, China). A custom-designed sensor mounter was printed by a Fused Deposition Modelling 3D printer (Ultimaker, Netherlands). Our pressure sensor was adhered to the mounter. The robotic arm and gripper were controlled by an M5Stack that received control commands from LabVIEW via serial communication. The sensor signals were received and processed in LabVIEW as was done in sensor characterization. The robot was placed inside a box, where the humidity was regulated using a humidifier. Note that due to larger noise in this setup, V_{spike} was filtered by a moving average filter. In the weight measurement experiment, the sensor was placed on top of a commercial load cell for comparison. The triboelectric sensor signals were received and processed using LabVIEW. The load cell was connected to an Arduino Mega, and the weight data was received via serial communication.

Supporting Information

Supporting Information is available from the Wiley Online Library or from the author.

Acknowledgements

C.H. and J.C. contributed equally to this work. This work was supported by the National Research Foundation (NRF) of Korea (2021R1A2C3008742). This work was also supported by Technological Innovation R&D Program (S3104117).

Conflict of Interest

The authors declare no conflict of interest.

Data Availability Statement

The data that support the findings of this study are available from the corresponding author upon reasonable request.

Keywords

self-powered sensors, triboelectric sensors, self-calibration, surface charge density

Received: July 20, 2023
Published online:

[1] Q. Wu, G. Y. Li, W. Chen, D. W. K. Ng, R. Schober, *IEEE Wireless Communications* **2017**, *24*, 72.
[2] F. Martins, C. Felgueiras, M. Smitková, *Energy Procedia* **2018**, *153*, 107.
[3] M. Cai, Z. Jiao, S. Nie, C. Wang, J. Zou, J. Song, *Sci. Adv.* **2019**, *7*, eabl8313.
[4] H. Yao, W. Yang, W. Cheng, Y. J. Tan, H. H. See, S. Li, H. P. A. Ali, B. Z. H. Lim, Z. Liuc, B. C. K. Tee, *Proc. Natl. Acad. Sci. USA* **2020**, *117*, 25352.
[5] G.-J. Zhu, P.-G. Ren, J. Wang, Q. Duan, F. Ren, W.-M. Xia, D.-X. Yan, *ACS Appl. Mater. Interfaces* **2020**, *12*, 19988.
[6] Y. Jung, J. Choi, W. Lee, J. S. Ko, I. Park, H. Cho, *Adv. Funct. Mater.* **2022**, *32*, 2201147.
[7] H. Han, Y. S. Oh, S. Cho, H. Park, S.-U. Lee, K. Ko, J.-M. Park, J. Choi, J.-H. Ha, C. Han, Z. Zhao, Z. Liu, Z. Xie, J.-S. Lee, W. G. Min, B.-J. Lee, J. Koo, D. Y. Choi, M. Je, J.-Y. Sun, I. Park, *Small* **2023**, *19*, 2205048.
[8] G.-J. Zhu, P.-G. Ren, H. Guo, Y.-L. Jin, D.-X. Yan, Z.-M. Li, *ACS Applied Materials & Interfaces* **2019**, *11*, 23649.
[9] S. Cho, H. Han, H. Park, S.-U. Lee, J.-H. Kim, S. W. Jeon, M. Wang, R. Avila, Z. Xi, K. Ko, M. Park, J. Lee, M. Choi, J.-S. Lee, W. G. Min, B.-J. Lee, S. Lee, J. Choi, J. Gu, J. Park, M. S. Kim, J. Ahn, O. Gul, C. Han, G. Lee, S. Kim, K. Kim, J. Kim, C.-M. Kang, J. Koo, et al., *npj Flexible Electronics* **2023**, *7*, 8.
[10] Q. Su, Q. Zou, Y. Li, Y. Chen, S.-Y. Teng, J. T. Kelleher, R. Nith, P. Cheng, N. Li, W. Liu, S. Dai, Y. Liu, A. Mazursky, J. Xu, L. Jin, P. Lopes, S. Wang, *Science Advances* **2021**, *7*, eabi4563.
[11] J. Choi, D. Kwon, K. Kim, J. Park, D. D. Orbe, J. Gu, J. Ahn, I. Cho, Y. Jeong, Y. Oh, I. Park, *ACS Appl. Mater. Interfaces* **2019**, *12*, 1698.
[12] K.-H. Ha, W. Zhang, H. Jang, S. Kang, L. Wang, P. Tan, H. Hwang, N. Lu, *Adv. Mater.* **2021**, *33*, 2103320.

[13] C. Lv, C. Tian, J. Jiang, Y. Dang, Y. Liu, X. Duan, Q. Li, X. Chen, M. Xie, *Adv. Sci.* **2023**, 2206807.
[14] Z. L. Wang, A. C. Wang, *Mater. Today* **2019**, *30*, 34.
[15] Y. Xu, W. Yang, X. Lu, Y. Yang, J. Li, J. Wen, T. Cheng, Z. L. Wang, *ACS Nano* **2021**, *15*, 16368.
[16] C. Zhang, L. Liu, L. Zhou, X. Yin, X. Wei, Y. Hu, Y. Liu, S. Chen, J. Wang, Z. L. Wang, *ACS Nano* **2020**, *14*, 7092.
[17] J. Ahn, J. S. Kim, Y. Jeong, S. Hwang, H. Yoo, Y. Jeong, J. Gu, M. Mahato, J. Ko, S. Jeon, J. H. Ha, H. S. Seo, J. Choi, M. Kang, C. Han, Y. Cho, C. H. Lee, J. H. Jeong, I. K. Oh, I. Park, *Adv. Energy Mater.* **2022**, *12*, 2201341.
[18] T. Jin, Z. Sun, L. Li, Q. Zhang, M. Zhu, Z. Zhang, G. Yuan, T. Chen, Y. Tian, X. Hou, C. Lee, *Nat. Commun.* **2020**, *11*, 1.
[19] T. Bu, T. Xiao, Z. Yang, G. Liu, X. Fu, J. Nie, T. Guo, Y. Pang, J. Zhao, F. Xi, C. Zhang, Z. L. Wang, *Adv. Mater.* **2018**, *30*, 1800066.
[20] G. Yao, L. Xu, X. Cheng, Y. Li, X. Huang, W. Guo, S. Liu, Z. L. Wang, H. Wu, *Advanced Functional Materials* **2020**, *30*, 1907312.
[21] S. Liu, Y. Li, W. Guo, X. Huang, L. Xu, Y.-C. Lai, C. Zhang, H. Wu, *Nano Energy* **2019**, *65*, 104005.
[22] H. Guo, X. Pu, J. Chen, Y. Meng, M.-H. Yeh, G. Liu, Q. Tang, B. Chen, D. Liu, S. Qi, C. Wu, C. Hu, J. Wang, Z. L. Wang, *Sci. Rob.* **2018**, *3*, eaat2516.
[23] X. Qu, Z. Liu, P. Tan, C. Wang, Y. Liu, H. Feng, D. Luo, Z. Li, Z. L. Wang, *Sci. Adv.* **2022**, *8*, eabq2521.
[24] S. Gao, T. He, Z. Zhang, H. Ao, H. Jiang, C. Lee, *Adv. Sci.* **2021**, *8*, 2101834.
[25] Q. Zhang, T. Jin, J. Cai, L. Xu, T. He, T. Wang, Y. Tian, L. Li, Y. Peng, C. Lee, *Adv. Sci.* **2022**, *9*, 2103694.
[26] G. Zhu, P. Ren, J. Yang, J. Hu, Z. Dai, H. Chen, Y. Li, Z. Li, *Nano Energy* **2022**, *98*, 107327.
[27] K. Meng, J. Chen, X. Li, Y. Wu, W. Fan, Z. Zhou, Q. He, X. Wang, X. Fan, Y. Zhang, J. Yang, Z. L. Wang, *Adv. Funct. Mater.* **2019**, *29*, 1806388.
[28] K. Dong, X. Peng, J. An, A. C. Wang, J. Luo, B. Sun, J. Wang, Z. L. Wang, *Nature Communications* **2020**, *11*, 2868.
[29] W. Fan, Q. He, K. Meng, X. Tan, Z. Zhou, G. Zhang, J. Yang, Z. L. Wang, *Science Advances* **2020**, *6*, eaay2840.
[30] Z. Yan, L. Wang, Y. Xia, R. Qiu, W. Liu, M. Wu, Y. Zhu, S. Zhu, C. Jia, M. Zhu, R. Cao, Z. Li, X. Wang, *Adv. Funct. Mater.* **2021**, *31*, 2100709.
[31] X. Yin, D. Liu, L. Zhou, X. Li, G. Xu, L. Liu, S. Li, C. Zhang, J. Wang, Z. L. Wang, *Adv. Funct. Mater.* **2020**, *30*, 2002547.
[32] J. Park, D.-H. Kang, H. Chae, S. K. Ghosh, C. Jeong, Y. Park, S. Cho, Y. Lee, J. Kim, Y. Ko, J. J. Kim, H. Ko, *Science Advances* **2020**, *8*,eabj9220.
[33] Q. He, Y. Wu, Z. Feng, W. Fan, Z. Lin, C. Sun, Z. Zhou, K. Meng, W. Wu, J. Yang, *J. Mater. Chem. A* **2019**, *7*, 26804.
[34] M. Zhu, Z. Sun, Z. Zhang, Q. Shi, T. He, H. Liu, T. Chen, C. Lee, *Sci. Adv.* **2020**, *6*, eaaz8693.
[35] X. Pu, M. Liu, X. Chen, J. Sun, C. Du, Y. Zhang, J. Zhai, W. Hu, Z. L. Wang, *Sci. Adv.* **2017**, *3*, 1700015.
[36] S. Wang, Y. Xie, S. Niu, L. Lin, C. Liu, Y. S. Zhou, Z. L. Wang, *Adv. Mater.* **2014**, *26*, 6720.
[37] N. Cui, L. Gu, Y. Lei, J. Liu, Y. Qin, X. Ma, Y. Hao, Z. L. Wang, *ACS Nano* **2016**, *10*, 6131.
[38] J. Wang, C. Wu, Y. Dai, Z. Zhao, A. Wang, T. Zhang, Z. L. Wang, *Nat. Commun.* **2017**, *8*, 1.
[39] D. W. Kim, J. H. Lee, I. You, J. K. Kim, U. Jeong, *Nano Energy* **2018**, *50*, 192.
[40] W. He, W. Liu, J. Chen, Z. Wang, Y. Liu, X. Pu, H. Yang, Q. Tang, H. Yang, H. Guo, C. Hu, *Nat. Commun.* **2020**, *11*, 1 .
[41] Y. Liu, W. Liu, Z. Wang, W. He, Q. Tang, Y. Xi, X. Wang, H. Guo, C. Hu, *Nat. Commun.* **2020**, *11*, 1.
[42] S. Niu, S. Wang, L. Lin, Y. Liu, Y. S. Zhou, Y. Hu, Z. L. Wang, *Energy Environ. Sci.* **2013**, *6*, 3576.
[43] V. Nguyen, Y. Rusen, *Nano Energy* **2013**, *2*,604.
[44] Q. Zhou, K. Lee, K. N. Kim, J. G. Park, J. Pan, J. Bae, J. M. Baik, T. Kim, *Nano Energy* **2019**, *57*, 903.
[45] J. Ahn, Z.-J. Zhao, J. Choi, Y. Jeong, S. Hwang, J. Ko, J. Gu, S. Jeon, J. Park, M. Kang, D. V. D. Orbe, I. Cho, H. Kang, M. Bok, J.-H. Jeong, I. Park, *Nano Energy* **2021**, *85*, 105978.
[46] J. Luo, Z. Wang, L. Xu, A. C. Wang, K. Han, T. Jiang, Q. Lai, Y. Bai, W. Tang, F. R. Fan, Z. L. Wang, *Nat. Commun.* **2019**, *10*, 1.
[47] Y.-T. Jao, P.-K. Yang, C.-M. Chiu, Y.-J. Lin, S.-W. Chen, D. Choi, Z.-H. Lin, *Nano Energy* **2018**, *50*, 513.
[48] K. Y. Lee, H.-J. Yoon, T. Jiang, X. Wen, W. Seung, S.-W. Kim, Z. L. Wang, *Adv. Energy Mater.* **2016**, *6*, 1502566.
[49] S. Liu, H. Wang, T. He, S. Dong, C. Lee, *Nano Energy* **2020**, *69*, 104462.
[50] G. Cheng, Z.-H. Lin, L. Lin, Z. Du, Z. L. Wang, *ACS Nano* **2013**, *7*, 7383.
[51] H.-J. Yoon, H. Ryu, S.-W. Kim, *Nano Energy* **2018**, *51*, 270.
[52] Q. Zheng, L. Fang, H. Guo, K. Yang, Z. Cai, M. A. B. Meador, S. Gong, *Adv. Funct. Mater.* **2018**, *28*, 1706365.
[53] D. A. Chernous, S. V. Shil'ko, *Mechanics of Composite Materials* **2005**, *41*, 415.
[54] P. Alam, D. Mamalis, C. Robert, C. Floreani, C. M. Ó Brádaigh, *Composites, Part B* **2008**, *166*, 555.
[55] L. S. McCarty, G. M. Whitesides, *Angew. Chem., Int. Ed.* **2008**, *47*, 2188.
[56] M. Sultan, H. Ashraf, T. Miyazaki, R. R. Shamshiri, I. A. Hameed, *Next-Generation Greenhouses for Food Security* **2021**.
[57] C. A. Campiotti, G. Morosinotto, G. Puglisi, E. Schettini, G. Vox, *Agriculture And Agricultural Science Procedia* **2016**, *8*, 664.
[58] B. Rabbi, Z.-H. Chen, S. Sethuvenkatraman, *Energies* **2019**, *12*, 2737.
[59] T. Wang, X. Xu, C. Wang, Z. Li, D. Li, *Agriculture* **2021**, *11*, 145.

